Supplementary Materials for:

Stability of the fcc phase in shocked nickel up to 332 GPa

Kimberly A. Pereira,[1] Samantha M. Clarke,[2]* Saransh Singh,[2] Richard Briggs,[2] Christopher P. McGuire,[2] Hae Ja Lee,[3] Dimitri Khaghani,[3] Bob Nagler,[3] Eric Galtier,[3] Eric Cunningham,[3] David McGonegle,[4,5] Sally J. Tracy,[6] Cara Vennari,[2] Martin G. Gorman,[2] Amy L. Coleman,[2] Carol Davis,[2] Trevor Hutchinson,[2] Jon H. Eggert,[2] Raymond F. Smith,[2] and James P. S. Walsh[1]*

1) Department of Chemistry, University of Massachusetts Amherst, Amherst, Massachusetts 01003, USA
2) Lawrence Livermore National Laboratory, 7000 East Avenue, Livermore, California 94501, USA
3) Linac Coherent Light Source, SLAC National Accelerator Laboratory, Menlo Park, California 94025, USA
4) Department of Physics, Clarendon Laboratory, University of Oxford, Oxford, OX1 3PU, UK
5) Atomic Weapons Establishment, Aldermaston, Reading, RG7 4PR, UK
6) Earth and Planets Laboratory, Carnegie Institution for Science, Washington, DC 20015, USA

*Corresponding authors:
clarke30@llnl.gov
jpswalsh@umass.edu

Journal Title

Table of Contents

Table S1. Description of melt lines cited in Figure 5. Full citation data is provided in the references section.

ID Code	Year of Publication	Description of Study	Reference
L93	1993	Experimental, Static	[1]
E01	2001	Experimental, Static	[2]
K03	2003	Computational	[3]
J05	2005	Experimental, Static	[4]
K06	2006	Computational	[5]
R07	2007	Computational	[6]
E13	2013	Experimental, Static	[7]
P13	2013	Computational	[8]
L14	2014	Experimental, Static	[9]
H14	2014	Computational	[10]
Z14	2014	Computational	[11]
M15	2015	Computational	[12]
C15	2015	Computational	[13]
B17	2017	Experimental, Static	[14]
Q19	2019	Computational	[15]
B20	2020	Computational	[16]
T22	2022	Computational	[17]
P23	2023	Computational	[18]
S23	2023	Computational	[19]

Table S2. Silicon transmission (SiT) of reported runs in the main text.

Run ID	SiT
097	30%
099	30%
160	20%
151	20%
420	35%
149	20%
422	20%
493	100%

Table S3. X-ray intensity percentages for preshot images.

Run ID	X-ray Percentage
096	10%
098	10%
159	10%
150	10%
419	2%
148	10%
421	2%
492	30%

Table S4. Pressure values determined by analysis of VISAR images and from density values using literature data [17].

Run ID	**Laser Intensity (W cm^{-2})**	**Stress from VISAR impedance matching (GPa)[a]**	**Pressure from measured density values (GPa) [a]**	**Pressure from calibration Equation (3) (GPa)**	**Observed compressed structure**	**Density (g cm^{-3})**
097	5.05×10^{12}	183±23	192±20	194±80	fcc	12.72(5)
099	7.37×10^{12}	240±18	274±19	249±75	fcc	13.44(1)
160	1.69×10^{13}	—	377±38	432±60	fcc	14.2(1)
151	1.82×10^{13}	—	486±35	454±64	fcc	14.92(2)
420	2.22×10^{13}	—	515±67	518±84	fcc	15.1(2)
422	2.23×10^{13}	—	531±52	519±84	fcc	15.2(1)
149	2.28×10^{13}	—	—	527±87	—	—

[a] Determined using a fit to literature data [21–28].

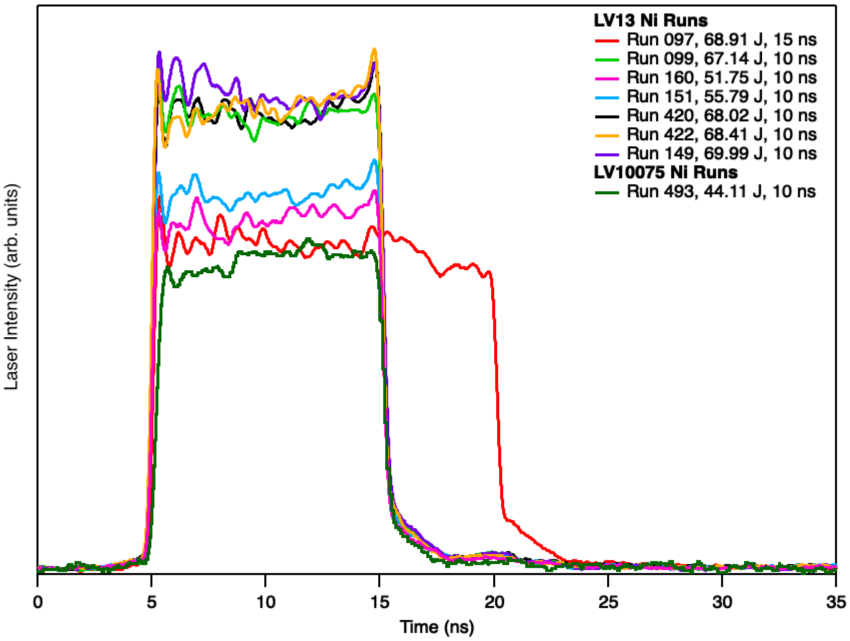

Figure S1. Plot of the laser drive pulse shapes for the eight runs discussed in this paper. The listed energy in Joules delivered for each run is a sum of the energy delivered by each of the four laser arms (AB, EF, GH, and IJ).

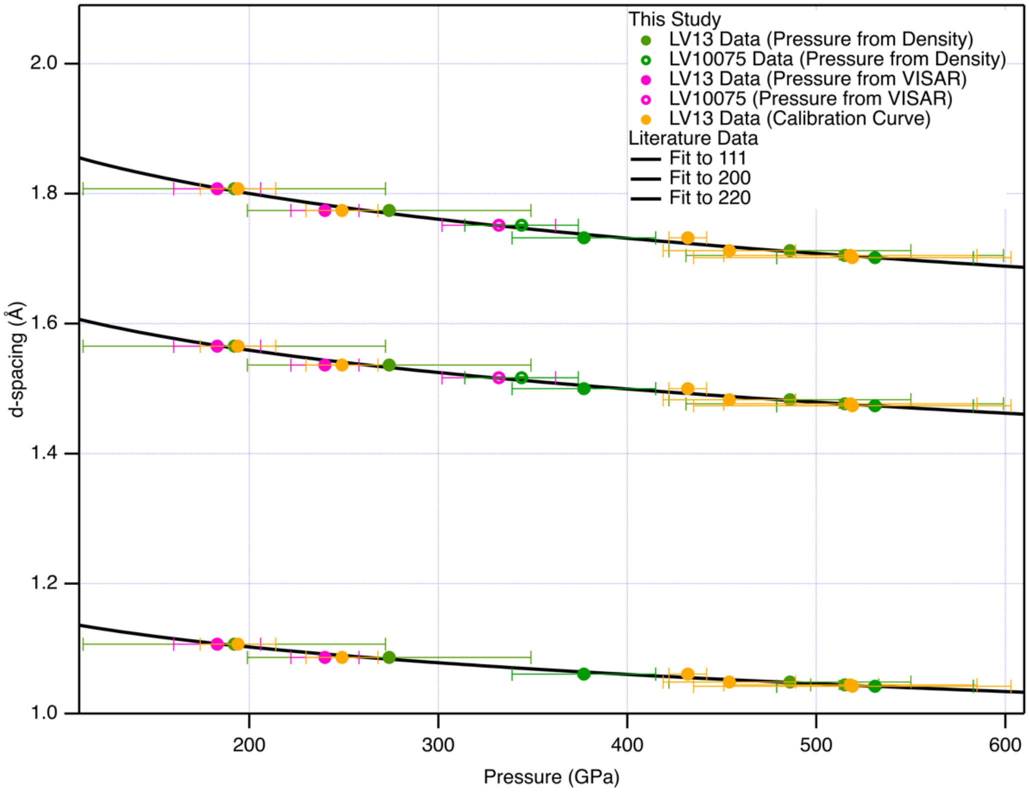

Figure S2. Plot of the *d*-spacing values obtained from independent peak position fitting (colored circles) along with the calculated *d*-spacing of these peaks assuming a cubic symmetry (black line). The pink circles correspond to pressures found via VISAR analysis for runs 097 and 099. The green circles represent pressure values derived from matching density values determined using Rietveld refinement of the X-ray diffraction data to states on the principal Ni Hugoniot SESAME 83103 from Ref. 17. The yellow circles represent pressures found using the laser intensity calibration curve described in the main text and depicted in Figure S14. The dependence of the *d*-spacing upon pressure was a least-squares fit calculated using literature data from [21–24,26–28].

S1. X-Ray Diffraction Measurements

The unique arrangement of the four ePix10k QUAD detectors necessitated careful handling of the X-ray diffraction data. Frequent pedestal images were collected over the course of the experiments to allow for correction of the drifting sensitivity of individual pixels over time, and these corrections were applied at the time of data collection [29]. The positions of the four ePix10k QUAD detectors were determined using a calibration pattern collected on CeO_2. Calibrations were performed individually for each detector using the *pyFAI-calib2* GUI, which was also used to create the masks for each detector. The calibration and mask files were used to perform a multi-geometry integration within *pyFAI*, which correctly matches the output space to the bin position and avoids artifacts in the integrated intensities that can arise when integrations are performed on individual detectors and then summed to create a single pattern. The *pyFAI* package also handles corrections for solid angle differences between individual pixels as well as corrections for polarization effects [30,31]. We found that the shot–to–shot X-ray energy varied on the order of 10–20 eV. To correct for these drifts, the uncompressed nickel was used as a pseudo-calibrant fixed to ambient lattice parameters, and the X-ray wavelength was allowed to refine to a best fit during Rietveld refinements.

A small signal from uncompressed fcc-Ni sample outside of the shocked region was observed in all runs performed throughout this experiment due to a diffuse halo of X-rays outside the center beam probe. This halo is estimated to be up to 250 μm in diameter, and contributes 2–4% to the ambient signal, with the rest of the ambient signal arising from uncompressed material ahead of the shock front. Since the LV13 experiment, this undesirable halo has been reduced at the MEC endstation through the addition of 100 μm slit collimators. A small ambient signal from the halo was still observed during the L10075 experiment. We did not correct for this signal. In all runs, the signal level from ambient reflections due to uncompressed material ahead of the shockwave is greater than the signal level arising from the halo effect.

To gain additional insight into the crystallinity of the samples before and during shock compression, we examined how the diffraction intensity varied along the azimuthal angle for the (111) and the (200) reflections before and after compression. Figure S11 shows the dewarped diffraction images recorded on detector Q3 for each shot from LV13 along with its corresponding preshot. The plots are all centered around the mean position of the reflections in question.

The (200) reflection was further analyzed in terms of the full width at half maximum (FWHM). In runs 097 and 099, the FWHM of the (200) reflection was around 0.8°, while for runs 160, 151, and 420, it increased to 0.9–1.1°. (Note that the (200) reflection in run 422 is very weak in intensity, most likely due to preferred orientation effects.) Although small, this broadening is consistent with what would be expected at the onset of melting, as noted in other studies [32].

Regarding the minimum melt detectability from X-ray diffraction measurements, we note that recent work at the Dynamic Compression Sector has estimated the minimum detectable melt by diffuse scattering diagnostic [33,34]. From the work on Ge, we understand that the minimum detectable is ~2 μm of liquid. Given that Ni is slightly lower Z than Ge, we expect that more liquid is needed. From the percent compressed data, we can determine that the shock transit through the sample in run 493 was ~10 μm. Extrapolating further, we estimate that our experimental diagnostic therefore would not detect the first 20–30% of melt. This could affect our understanding of the coexistence between liquidus and solidus in the Ni system (an issue that incidentally would also affect Fe melting studies that rely upon X-ray diffraction, given the similarity in *Z*). We note, however, that since our experimental techniques are much more sensitive to solid crystalline structures, we can place full confidence in the last observation of solid single-phase fcc-Ni. The uncertainty in the onset of melting could make our data consistent with some of the steepest melt curves proposed in the literature, but is clearly not sufficient to support the much shallower curves.

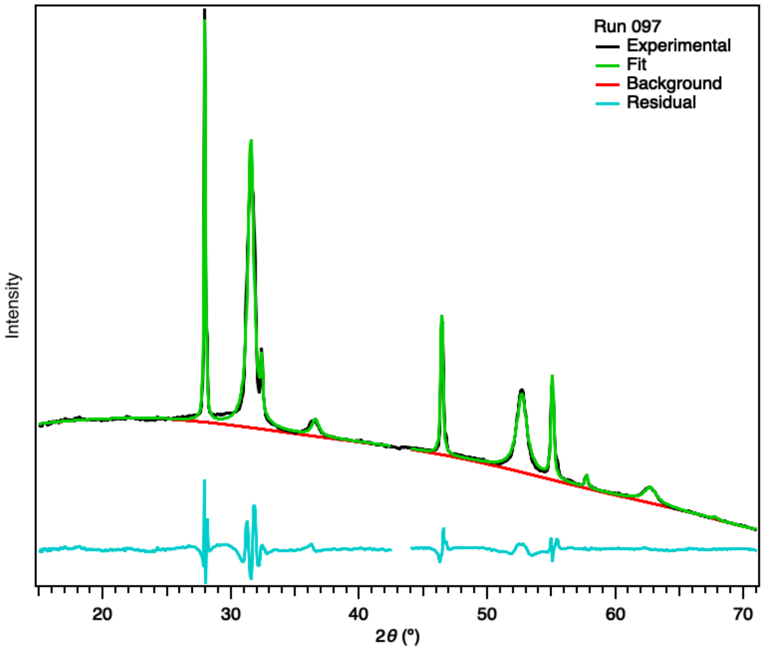

Figure S3. Rietveld fit to the X-ray diffraction data collected during Run 097. Plot shows the experimental data (black trace), simulated intensity (green trace), background function (red trace), and the unscaled residual (light blue trace). The multidetector setup at the Matter in Extreme Conditions instrument leads to small steps in the background at some of the detector edges. To minimize their influence on the fits, regions of 2*θ* with prominent background steps were excluded in the Rietveld refinement. These regions can be seen as gaps in the model traces.

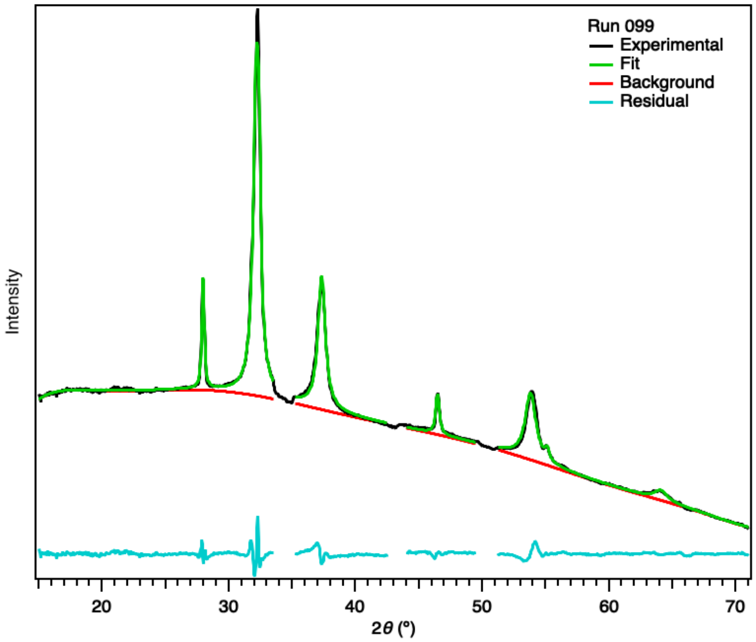

Figure S4. Rietveld fit to the X-ray diffraction data collected during Run 099. Plot shows the experimental data (black trace), simulated intensity (green trace), background function (red trace), and the unscaled residual (light blue trace). The multidetector setup at the Matter in Extreme Conditions instrument leads to small steps in the background at some of the detector edges. To minimize their influence on the fits, regions of 2*θ* with prominent background steps were excluded in the Rietveld refinement. These regions can be seen as gaps in the model traces.

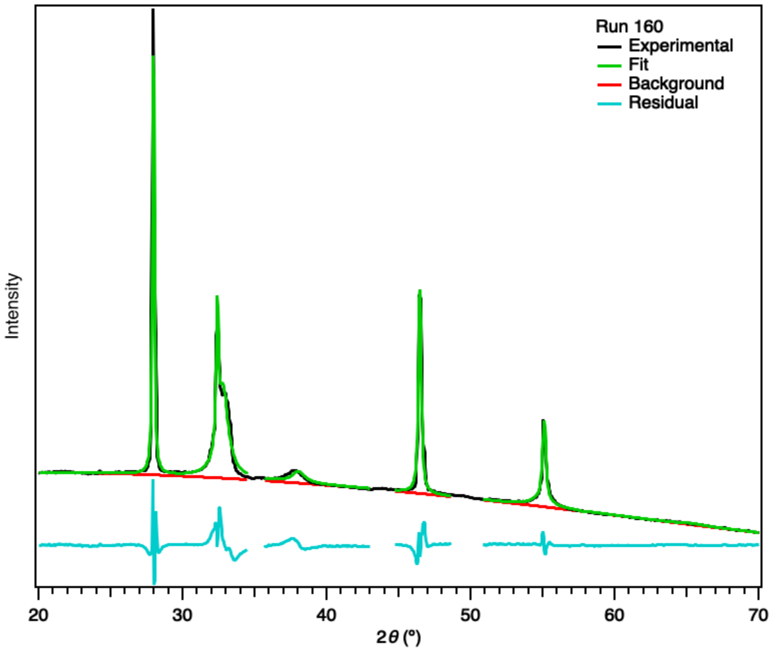

Figure S5. Rietveld fit to the X-ray diffraction data collected during Run 160. Plot shows the experimental data (black trace), simulated intensity (green trace), background function (red trace), and the unscaled residual (light blue trace). The multidetector setup at the Matter in Extreme Conditions instrument leads to small steps in the background at some of the detector edges. To minimize their influence on the fits, regions of 2*θ* with prominent background steps were excluded in the Rietveld refinement. These regions can be seen as gaps in the model traces.

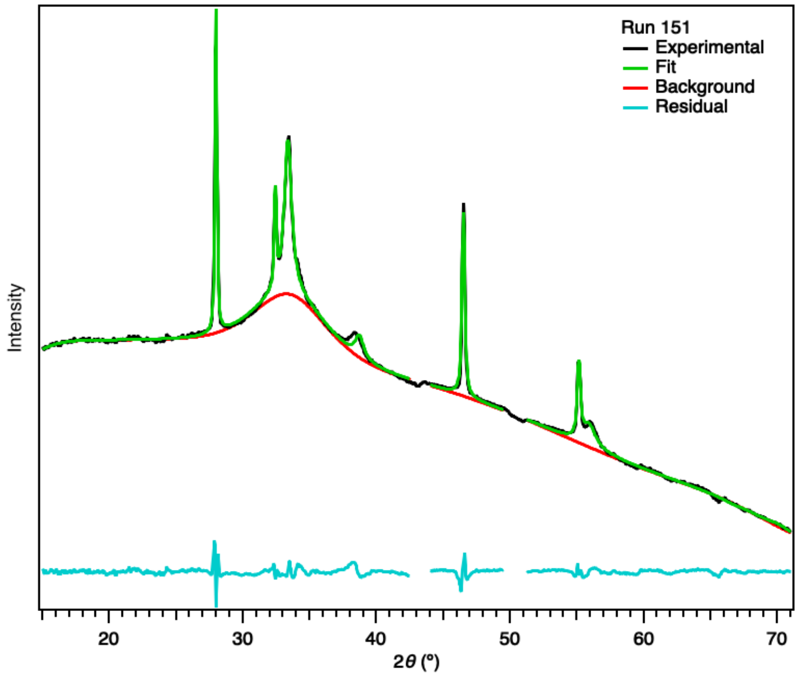

Figure S6. Rietveld fit to the X-ray diffraction data collected during Run 151. Plot shows the experimental data (black trace), simulated intensity (green trace), background function (red trace), and the unscaled residual (light blue trace). The multidetector setup at the Matter in Extreme Conditions instrument leads to small steps in the background at some of the detector edges. To minimize their influence on the fits, regions of 2*θ* with prominent background steps were excluded in the Rietveld refinement. These regions can be seen as gaps in the model traces.

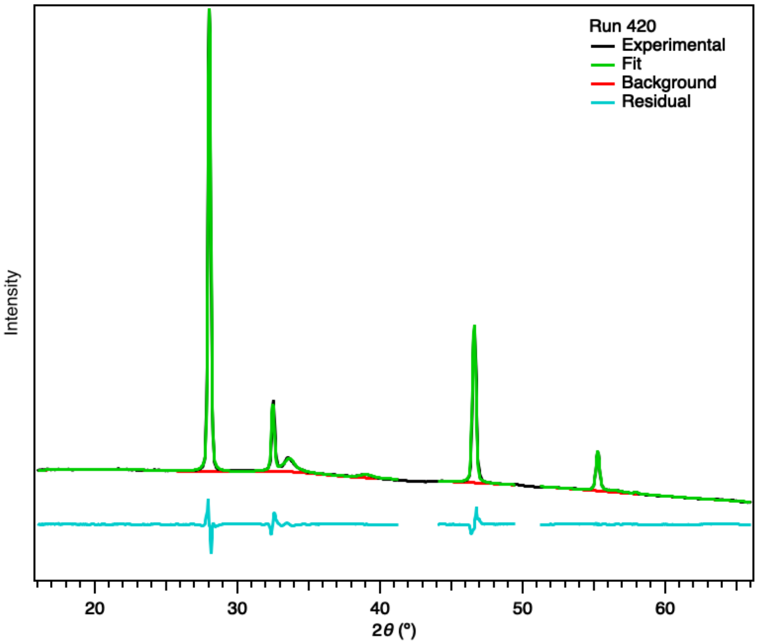

Figure S7. Rietveld fit to the X-ray diffraction data collected during Run 420. Plot shows the experimental data (black trace), simulated intensity (green trace), background function (red trace), and the unscaled residual (light blue trace). The multidetector setup at the Matter in Extreme Conditions instrument leads to small steps in the background at some of the detector edges. To minimize their influence on the fits, regions of 2*θ* with prominent background steps were excluded in the Rietveld refinement. These regions can be seen as gaps in the model traces.

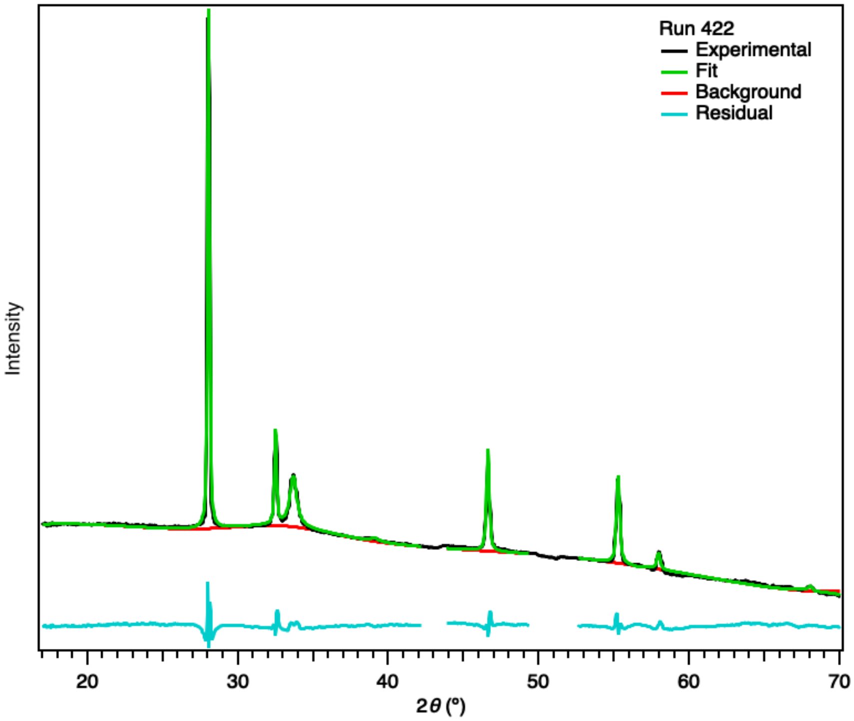

Figure S8. Rietveld fit to the X-ray diffraction data collected during Run 422. Plot shows the experimental data (black trace), simulated intensity (green trace), background function (red trace), and the unscaled residual (light blue trace). The multidetector setup at the Matter in Extreme Conditions instrument leads to small steps in the background at some of the detector edges. To minimize their influence on the fits, regions of 2θ with prominent background steps were excluded in the Rietveld refinement. These regions can be seen as gaps in the model traces.

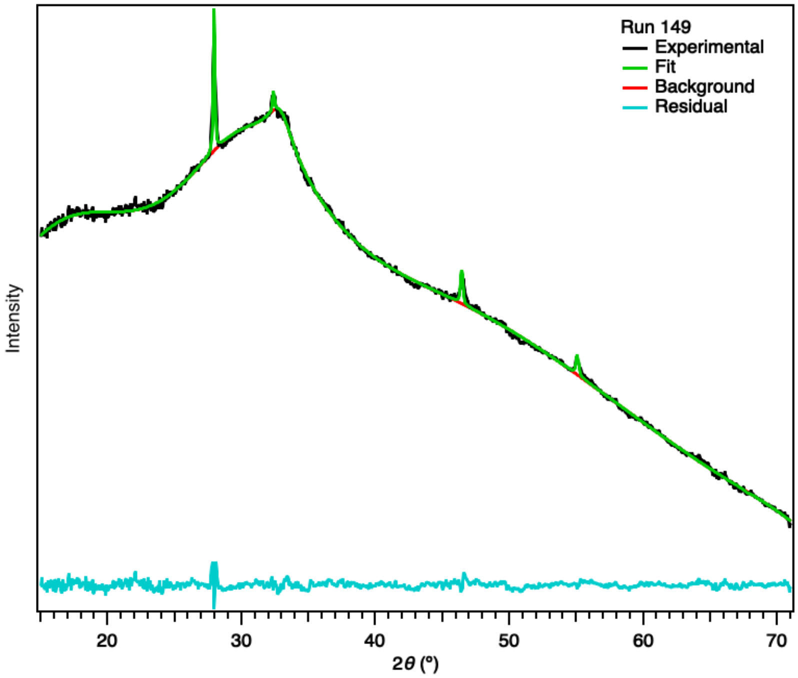

Figure S9. Rietveld fit to the X-ray diffraction data collected during Run 149. Plot shows the experimental data (black trace), simulated intensity (green trace), background function (red trace), and the unscaled residual (light blue trace).

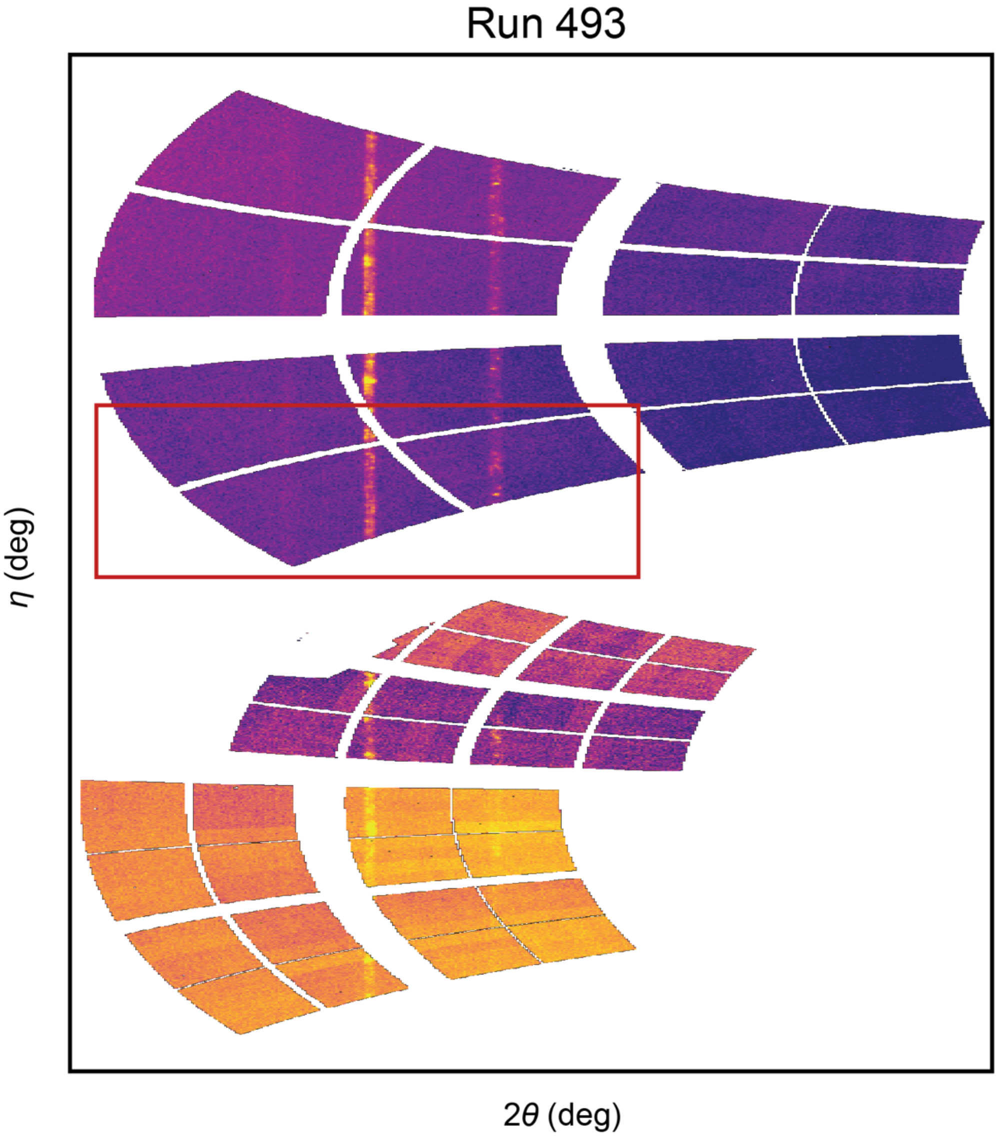

Figure S10. Cake plot of the X-ray diffraction data collected during Run 493. Quad 2 is not shown as it did not capture any useful diffraction. Plot shows the experimental data and the region used in integration (red rectangle): η = 10–50° and 2θ = 22–63°.

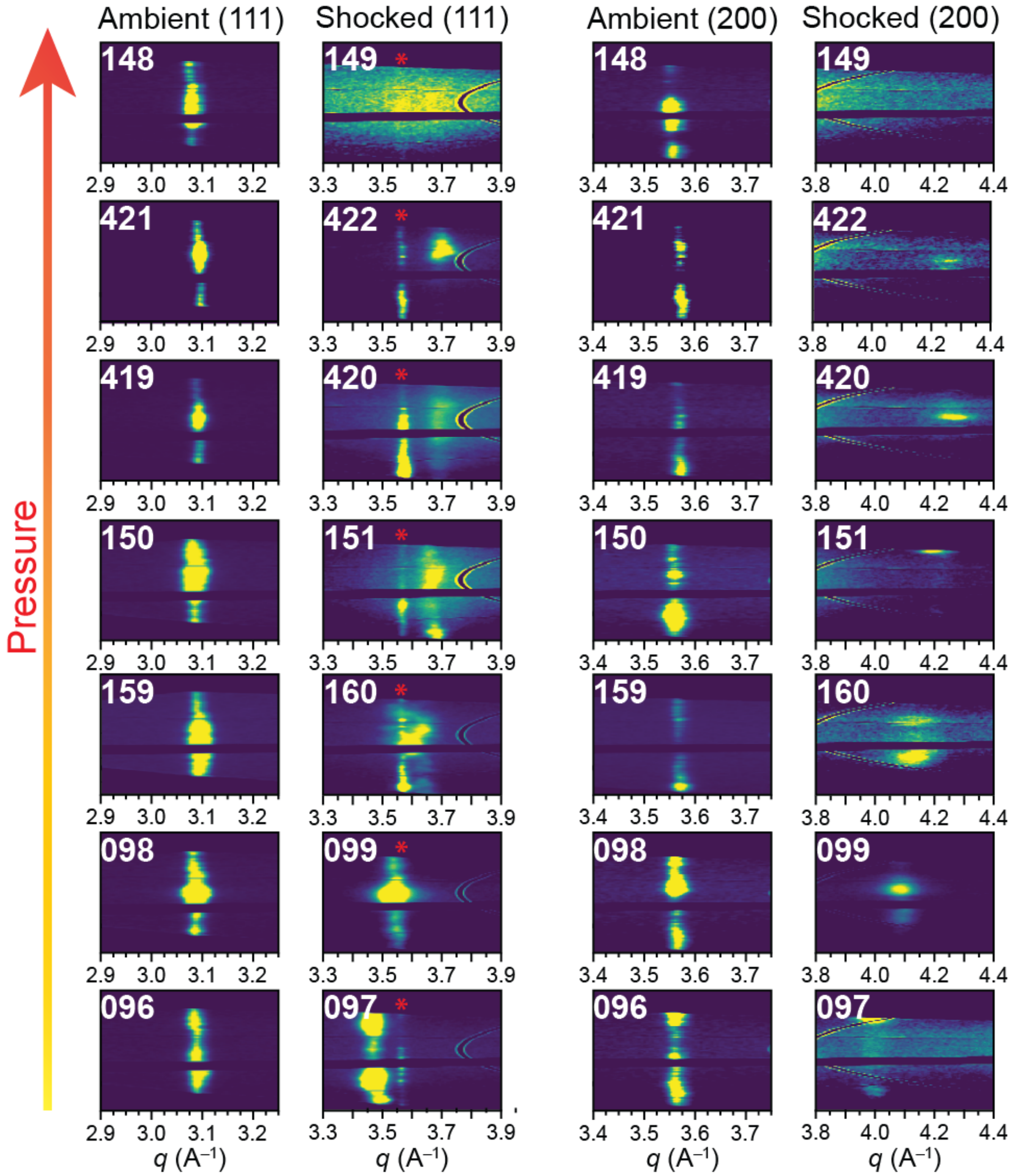

Figure S11. Left: Dewarped diffraction images showing the (111) texture at ambient conditions (preshot) alongside the (111) texture in the compressed phase measured during the shots. The vertical axis ranges from azimuthal angle ϕ 130° to 230° The run numbers are printed in the upper left corner of each image. The red asterisks indicate the ambient (200) peak present in the diffraction images. Right: Dewarped diffraction images showing the (200) texture at ambient conditions (preshot) alongside the (200) texture in the compressed phase measured during the shots. The vertical axis ranges from azimuthal angle ϕ 130° to 230°.

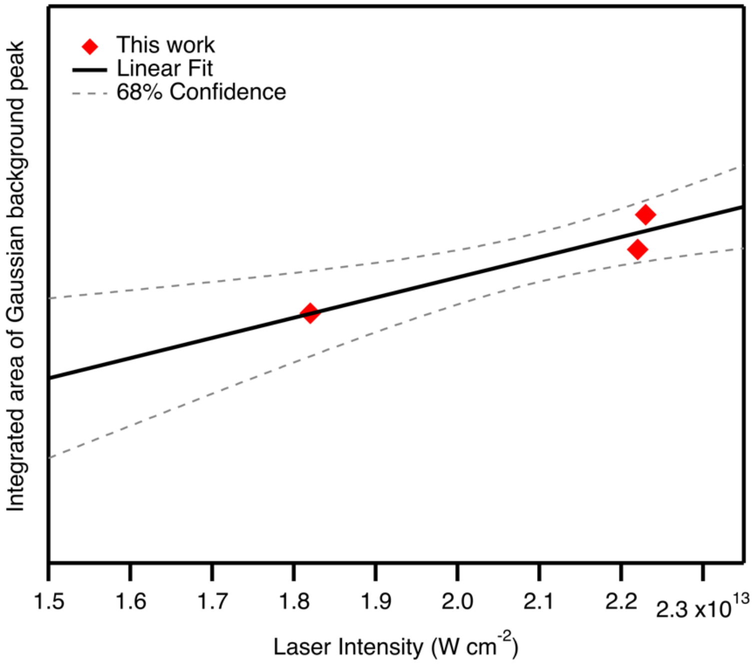

Figure S12. The integrated area of the Gaussian background peak in the X-ray diffraction for Runs 151, 420, and 422 is plotted against the laser intensity for each of these shots. We note that the difference in X-ray intensity noted in Table S4 and Table S5 has been accounted for in these calculations, and that the integrated area has been scaled to account for different amounts of compressed sample.

S2. Laser Intensity Calibration Curves

In the main manuscript, we report a laser intensity calibration curve relating pressure in the Ni sample to the laser intensity for each shot. This calibration curve was constructed using pressure values obtained by correlating density values of the compressed phase derived from Rietveld refinement to pressure using the SESAME 83103 Hugoniot [17]. We note that other runs not discussed in this paper (095, 158, and 351) are used in this calibration curve (See Figure S13). The diffractograms associated with these runs were analyzed and, using Rietveld refinement, we identified one compressed and one ambient phase. The data for these runs is summarized in Table S1 below. No release phases were observed in these runs. We considered the data valid to include in the calibration curve. Other runs not mentioned in this paper that contained release fell below our calibration curve.

Table S6. Data for runs 095, 158, and 351 with nickel densities determined from Rietveld refinements. Pressure values were calculated using equations of state from the SESAME database (83103 for Ni [17]).

Run	CH Thickness (µm)	Ni Thickness (µm)	Density of compressed phase (g cm^{-3})	Pressure in Ni layer (GPa)
095	80	22	12.61(3)	181(15)
158	80	22	14.16(2)	371(26)
351	80	22	9.21(4)	8.5(7)

We have also investigated the utility of a laser intensity calibration curve based on measured polyimide stresses in separate experiments performed on targets containing only polyimide and a window, with no sample layer. The particle velocity measured at the polyimide–window interface was used to determine the peak stress in the polyimide for a prescribed laser intensity, and these data were fit with an equation of the form proposed by Drake and Lindl [35–37]. These fits are shown in Figure S13 and S14, and the equation is given below. We opted to calibrate against data measured with 150–300 µm phase plates and 10–15 ns pulses, which cover the parameters used in our experiments.

$$P_{polyimide}[GPa] = 979.58(\pm 173)\left(\frac{I\left[\frac{PW}{cm^2}\right]}{0.527\ \mu m}\right)^{0.57593(\pm 0.0379)}$$

Equation S1.

For the two lowest intensity runs, the stresses calculated from this calibration curve agree well with the stresses determined from impedance matching and stress–density relationships. However, because the maximum laser intensity in our calibration dataset was 1.35x10^{13} W/cm^2, it may not be reliable for runs 158, 160, 151, 420, and 149, which require a significant extrapolation.

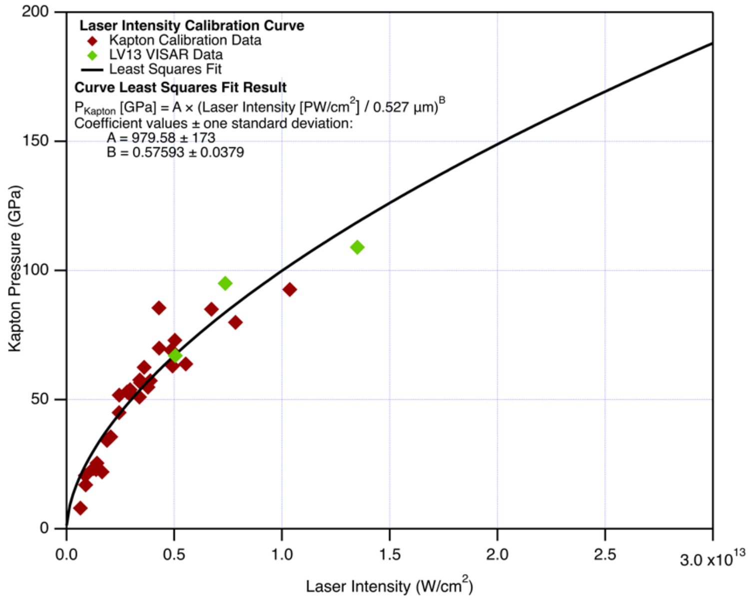

Figure S13. Plot of the pressures determined from VISAR collected from targets with only Kapton/LiF from separate experiments performed by the authors (filled maroon diamonds), along with pressures determined from Runs 097, 099, and 156 (filled green diamonds), both plotted versus laser intensity. (Note: Run 156, which is not discussed in this manuscript, yielded XRD and VISAR data. The VISAR data suggested a pressure of 109 GPa in the Kapton through impedance matching). Black trace shows a fit to the data using the equation detailed Drake and Lindl [35–37]. The equation is detailed in the legend, along with values for the fitted coefficients A and B.

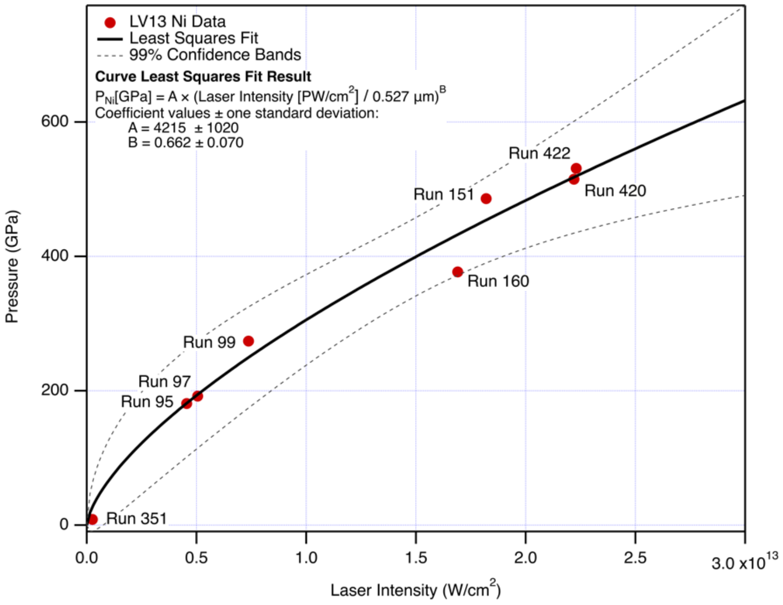

Figure S14. Plot of the nickel pressures determined from X-ray diffraction versus laser intensity. Black trace shows a fit to the data using the equation proposed Drake and Lindl [35–37]. The equation is detailed in the legend, along with values for the fitted coefficients A and B.

S3. Effect of Glue Layers

We investigated the effect of thick glue layers (≥5 μm) on the shocked states produced in the sample using the 1D hydrodynamic simulations package HYADES. [39] We observed that a thick front glue layer experiences a reverberating shock that produces two compressed phases in the Ni material of interest. At early probe times (before 25% sample compression for a 5 μm glue layer and 50% sample compression for a 10 μm glue layer), both compressed phases are present. However, neither are Hugoniot phases. At later probe times (after 25% sample compression for a 5 μm glue layer and 50% sample compression for a 10 μm glue layer, the faster reverberating shockwave catches up to and rejoins the slower original shockwave in the sample, creating one steady single shock. This shockwave produces a third compressed state, which is a Hugoniot state. Of note is the increased temperature of this third compressed state, which is about 500-600 K hotter than the first two compressed states. As a result, probing at later times is desired to observe the compressed Hugoniot state.

We also explored the effect of thick rear glue layers on the sample. After breakout, the pressure is released in the sample. However, a reverberating shockwave in the rear glue layer will lead to a second release wave. This results in two release states: the first from the release wave, and the second from the reverberated release wave. The first release state is a lowest density in Nickel than the second release state. According to simulations performed without glue layers where the on-compression Hugoniot state was reproduced, the second release state most closely matches the expected isentropic release state. Therefore, probing the sample at early times post-breakout will yield a mix of signals from both release states.

The findings of simulations incorporating glue layers are represented in Figure S15 below. By pausing the simulation at various times, it is possible to assess which phases would be present if the X-ray probe was delivered at that time.

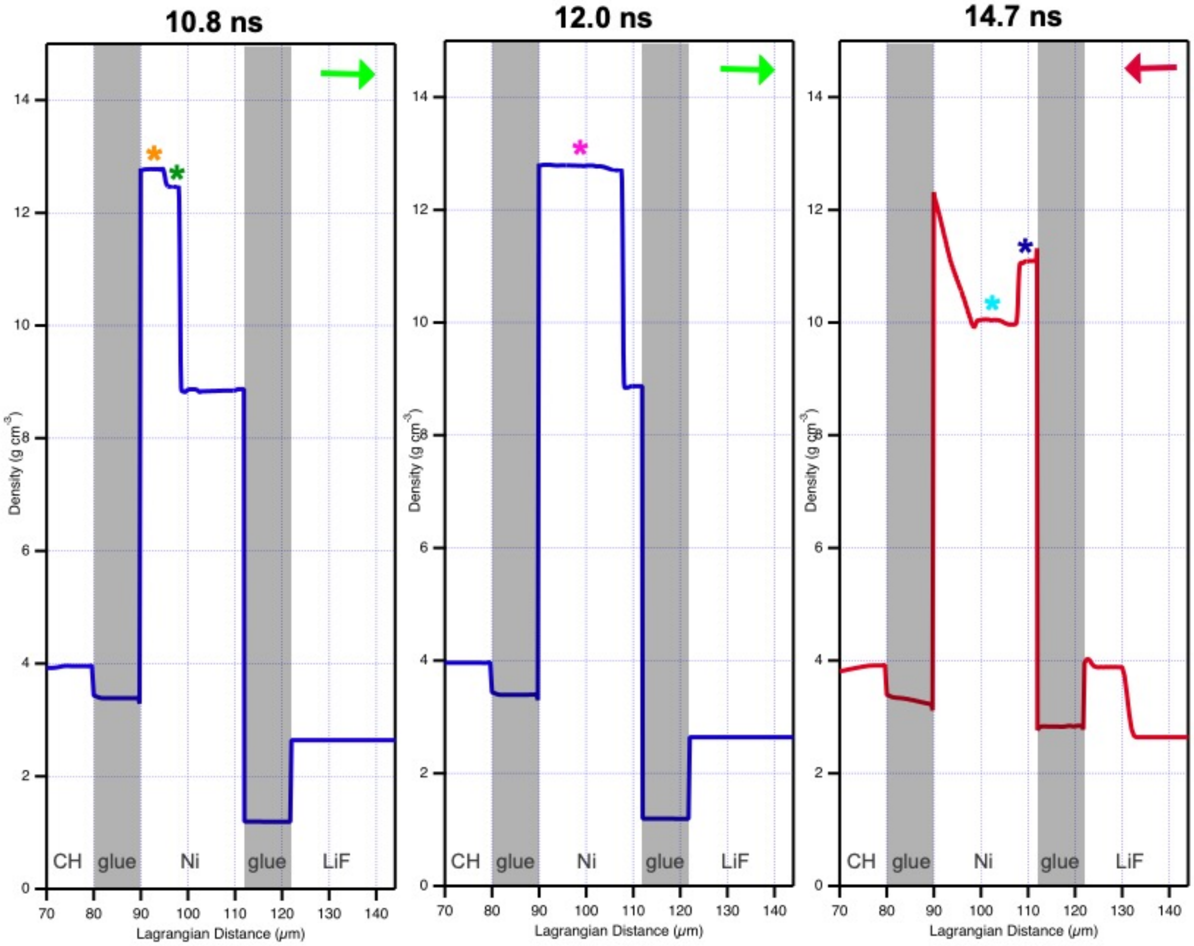

Figure S15. HYADES simulations of a Ni sample under compression viewed as distance into the sample versus density (see Ref. 39 for information on HYADES). Arrows in the upper right-hand corner of each pane show the direction of the shock, with green signaling the simulation is on compression, and red signaling the simulation is on release. Left) At early times, two compressed phases are present. Compressed state 1, denoted with an orange asterisk, has the following physical characteristics: ρ = 12.77 g cm^{-3}, P = 180 GPa, and T = 2,945 K. Compressed state 2, denoted with a green asterisk, has the following physical characteristics: ρ = 12.45 g cm^{-3}, P = 159 GPa, and T = 2,845 K. Neither of these states are Hugoniot states. Middle) At later times, when the sample is greater than 50% compressed, one state is present. Compressed state 3, denoted with a pink asterisk, has the following physical characteristics: ρ = 12.72 g cm^{-3}, P = 181 GPa, and T = 3,450 K. This is the Hugoniot shocked state. Right) Post-breakout, two release states can be observed. Release state 1, denoted with a teal asterisk, has the following physical characteristics: ρ = 10.02 g cm^{-3}, P = 43 GPa, and T = 2,262 K. Release state 2, denoted with a blue asterisk, has the following physical characteristics: ρ = 11.09 g cm^{-3}, P = 88 GPa, and T = 2,743 K. Release state 2 most closely matches with the expected isentropic release state. Simulations were conducted with SESAME EOS 83103 for Ni and SESAME EOS 7602 for the epoxy [17,20].

We also explored the effect of glue layers on VISAR data. We observe that a step feature is produced in the time vs. particle velocity plot achieved by analyzing VISAR data. Figure S16 demonstrates the appearance of this step as a result of 10 μm glue layers. We have found that the second plateau, indicated with a green box, corresponds to the Hugoniot state in the LiF layer. Interpreting this region as the Hugoniot state arose from simulations performed with the same experimental conditions, but without glue layers. We have applied this understanding to the interpretation of experimental VISAR data in this paper.

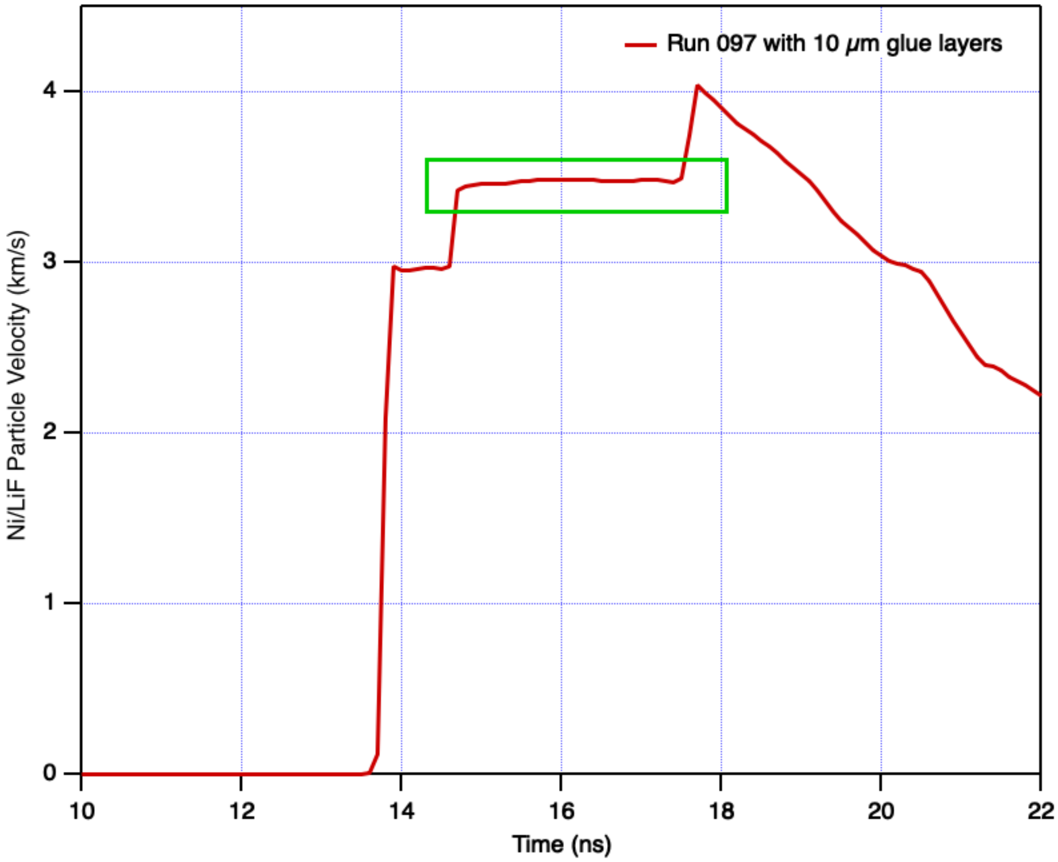

Figure S16. Simulation of particle velocity versus time at the Ni/LiF interface for Run 097 using the HYADES package. This simulation incorporates two 10 μm glue layers: one before the Ni layer, and one after the Ni layer and before the LiF window. Breakout occurs at the sharp increase in particle velocity, followed by a plateau, and then followed by a second plateau. The second plateau, indicated with a green box, corresponds to the Hugoniot state. Simulations were calculated using equations of state from the SESAME database (83103 for Ni [17], 7271 for LiF and 7770 for Kapton [20]).

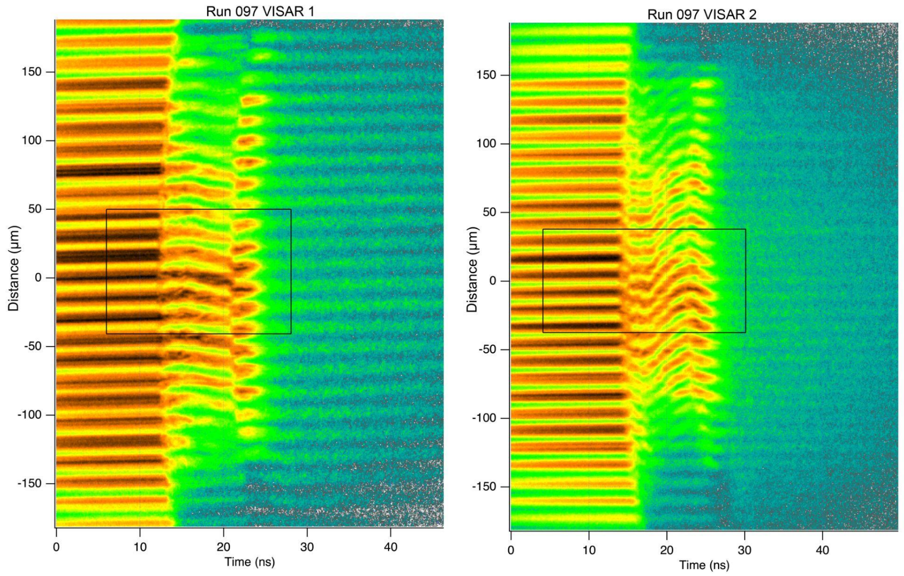
Run 097 VISAR 1

Run 097 VISAR 2

Figure S17. Streak camera output for Run 097. Left: Line VISAR 1; Right: Line VISAR 2. The *y*-axis plots distance, calibrated to account for the field of view and centered at zero. The *x*-axis represents the time from laser start and relies on timing calibration data available from MEC. The rectangles in each image correspond to the area integrated in our analysis, and has a height that approximates to the size of the probe X-ray beam.

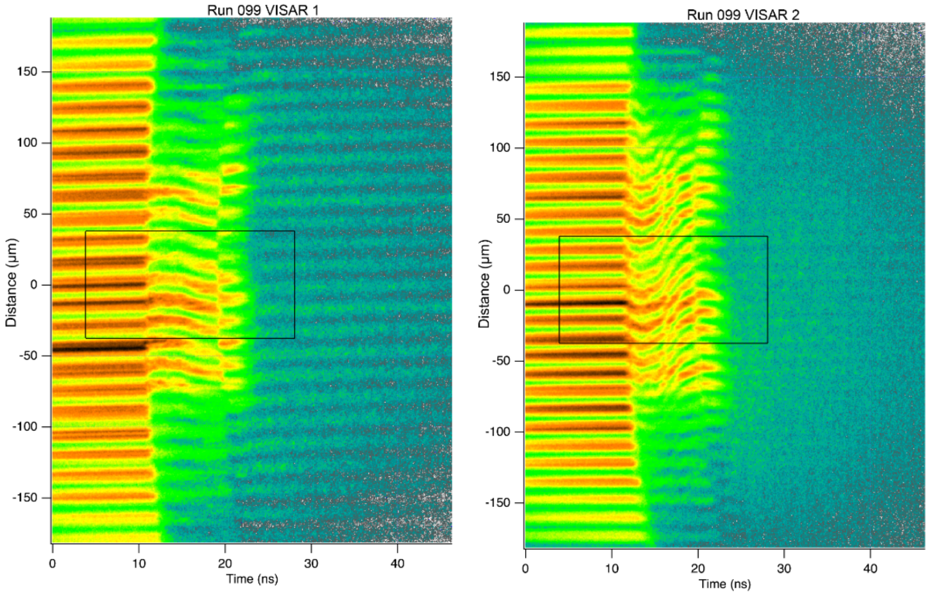
Run 099 VISAR 1

Run 099 VISAR 2

Figure S18. Streak camera output for Run 099. Left: Line VISAR 1; Right: Line VISAR 2. The *y*-axis plots distance, calibrated to account for the field of view and centered at zero. The *x*-axis represents the time from laser start and relies on timing calibration data available from MEC. The rectangles in each image correspond to the area integrated in our analysis, and has a height that approximates to the size of the probe X-ray beam.

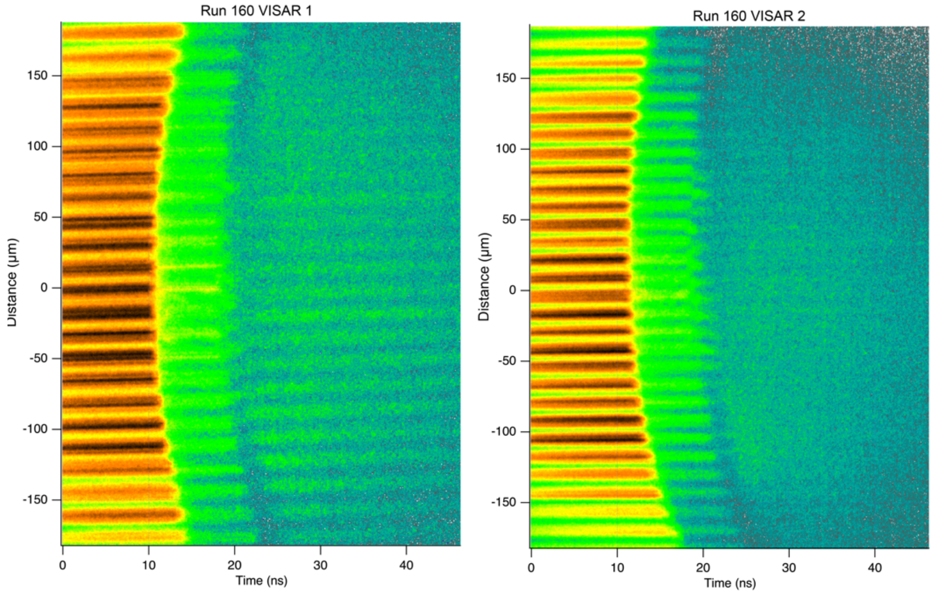

Figure S19. Streak camera output for Run 160. Left: Line VISAR 1; Right: Line VISAR 2. The *y*-axis plots distance, calibrated to account for the field of view and centered at zero. The *x*-axis represents the time from laser start and relies on timing calibration data available from MEC.

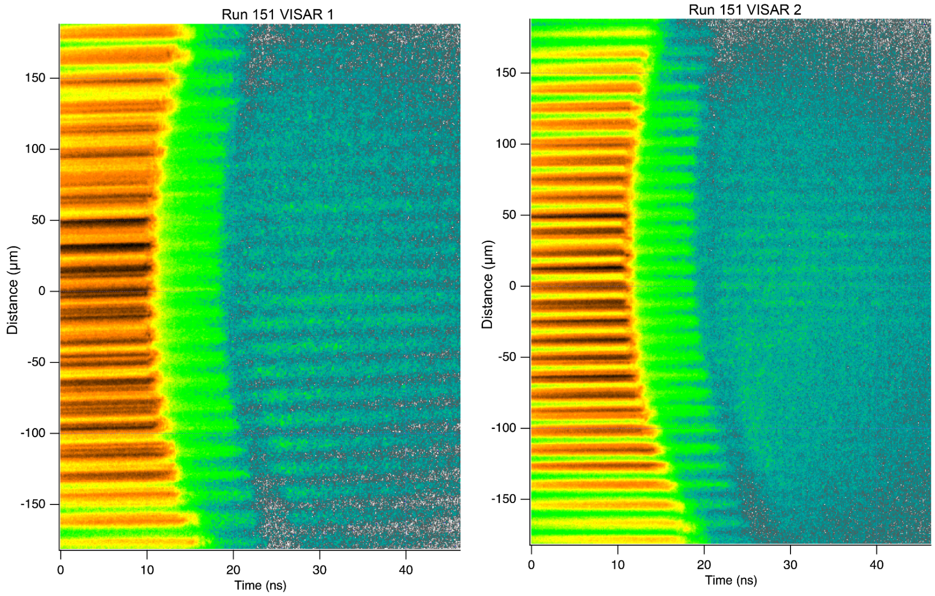

Figure S20. Streak camera output for Run 151. Left: Line VISAR 1; Right: Line VISAR 2. The *y*-axis plots distance, calibrated to account for the field of view and centered at zero. The *x*-axis represents the time from laser start and relies on timing calibration data available from MEC.

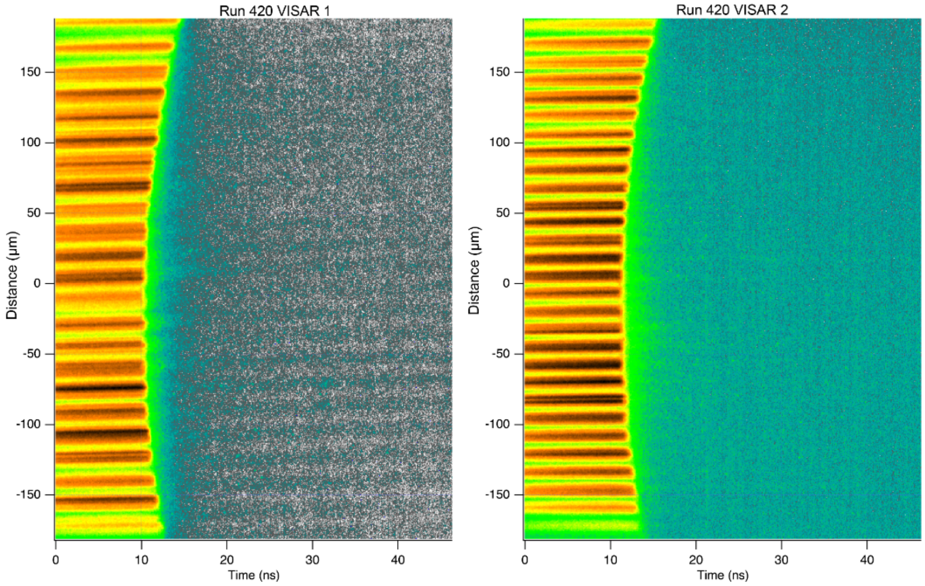

Figure S21. Streak camera output for Run 420. Left: Line VISAR 1; Right: Line VISAR 2. The *y*-axis plots distance, calibrated to account for the field of view and centered at zero. The *x*-axis represents the time from laser start and relies on timing calibration data available from MEC.

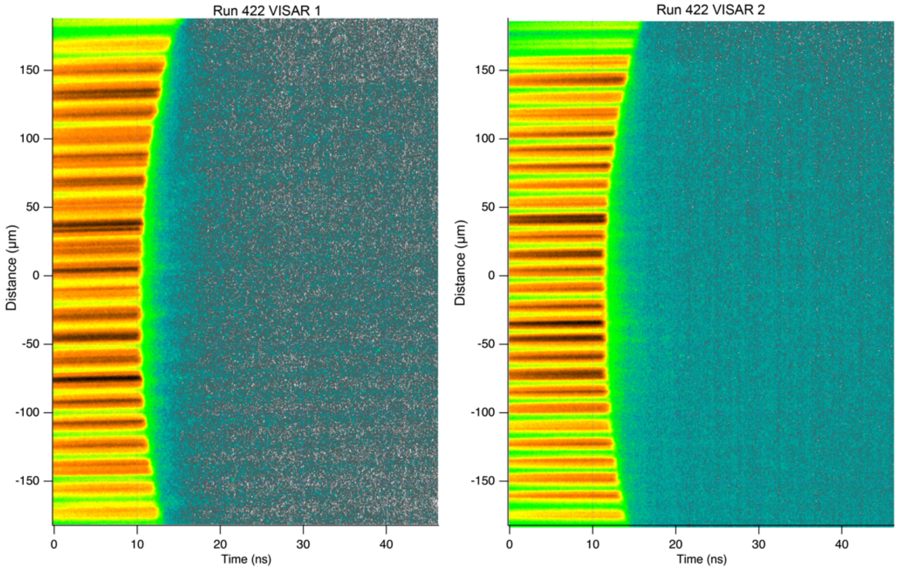

Figure S22. Streak camera output for Run 422. Left: Line VISAR 1; Right: Line VISAR 2. The *y*-axis plots distance, calibrated to account for the field of view and centered at zero. The *x*-axis represents the time from laser start and relies on timing calibration data available from MEC.

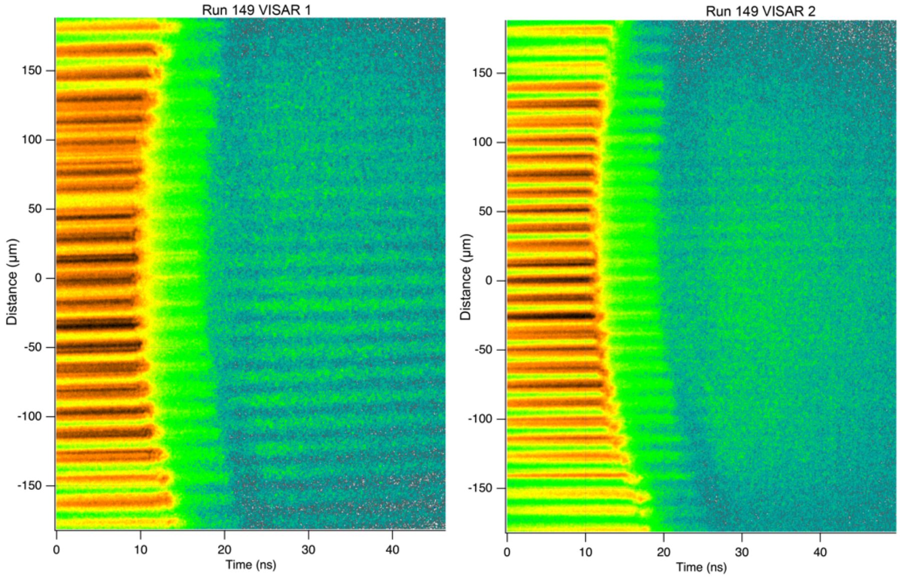

Figure S23. Streak camera output for Run 149. Left: Line VISAR 1; Right: Line VISAR 2. The *y*-axis plots distance, calibrated to account for the field of view and centered at zero. The *x*-axis represents the time from laser start and relies on timing calibration data available from MEC.

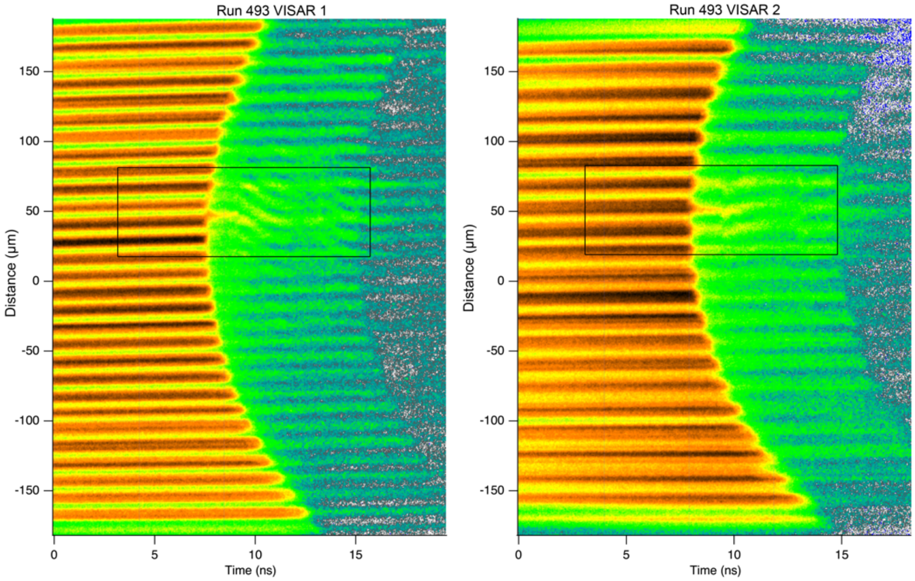

Figure S24. Streak camera output for Run 493. Left: Line VISAR 1; Right: Line VISAR 2. The *y*-axis plots distance, calibrated to account for the field of view and centered at zero. The *x*-axis represents the time from laser start and relies on timing calibration data available from MEC. The rectangles in each image correspond to the area integrated in our analysis, and has a height that approximates to the size of the probe X-ray beam.

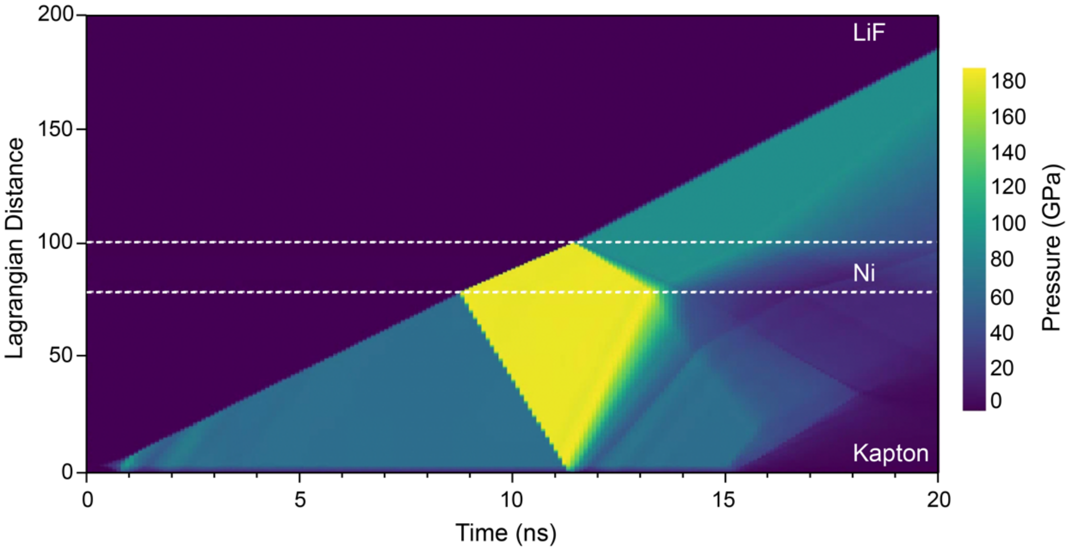

Figure S25. Plot of the 1D hydrocode simulations carried out for Run 097 using the HYADES package. Different layers of the sample are labelled, with dashed white lines denoting the interfaces. The simulations were designed to match the density obtained from the Rietveld refinements of the X-ray diffraction data. Pressures reached in the sample are plotted by color, with the corresponding color bar legend shown on the right. Simulations were calculated using equations of state from the SESAME database (83103 for Ni [17], 7271 for LiF and 7770 for Kapton [20]).

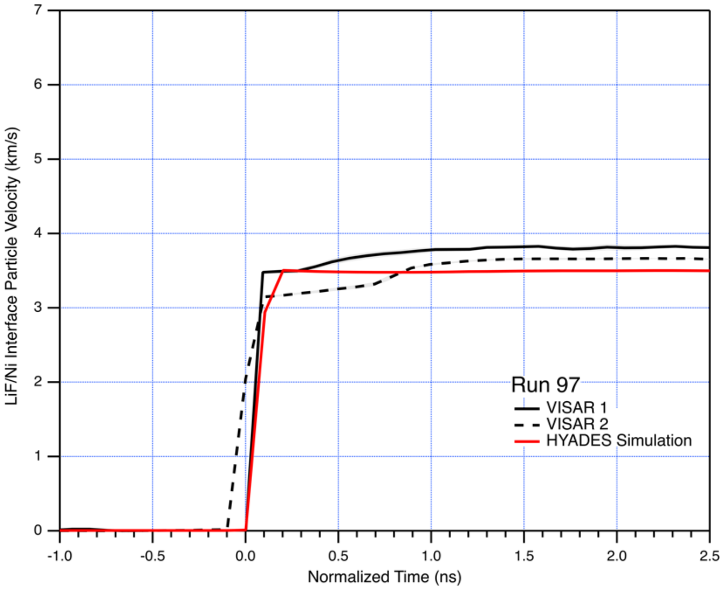

Figure S26. Comparison of experimental VISAR data with calculated particle velocity for the Ni compressed state with a density of 12.72 g/cm^3 (refined from the XRD data). Simulation of particle velocity versus time at the Ni/LiF interface for Run 097 uses the HYADES package. Breakout occurs at the sharp increase in particle velocity, followed by a plateau. Simulations were calculated using equations of state from the SESAME database (83103 for Ni [17], 7271 for LiF and 7770 for Kapton [20]).

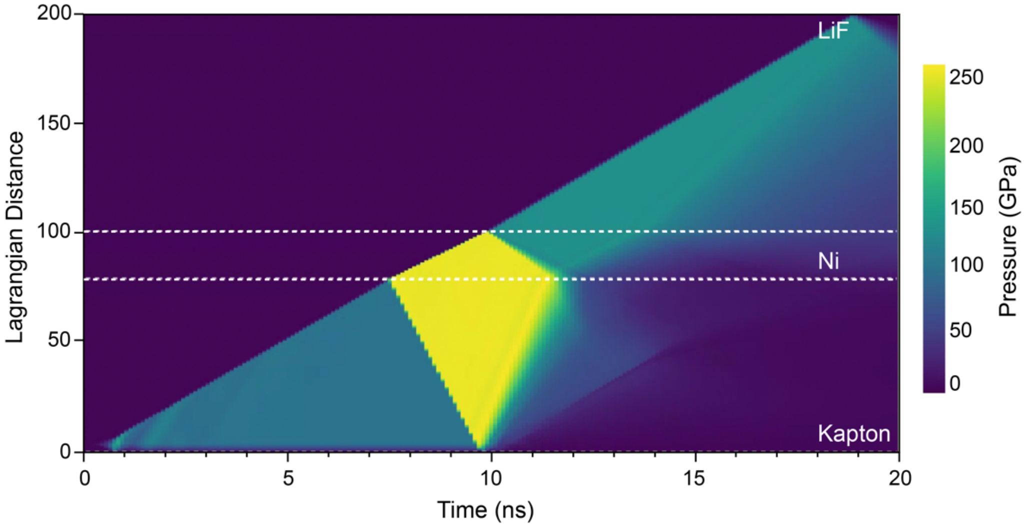

Figure S27. Plot of the 1D hydrocode simulations carried out for Run 099 using the HYADES package. Different layers of the sample are labelled, with dashed white lines denoting the interfaces. The simulations were designed to match the density obtained from the Rietveld refinements of the X-ray diffraction data. Pressures reached in the sample are plotted by color, with the corresponding color bar legend shown on the right. Simulations were calculated using equations of state from the SESAME database (83103 for Ni [17], 7271 for LiF and 7770 for Kapton [20]).

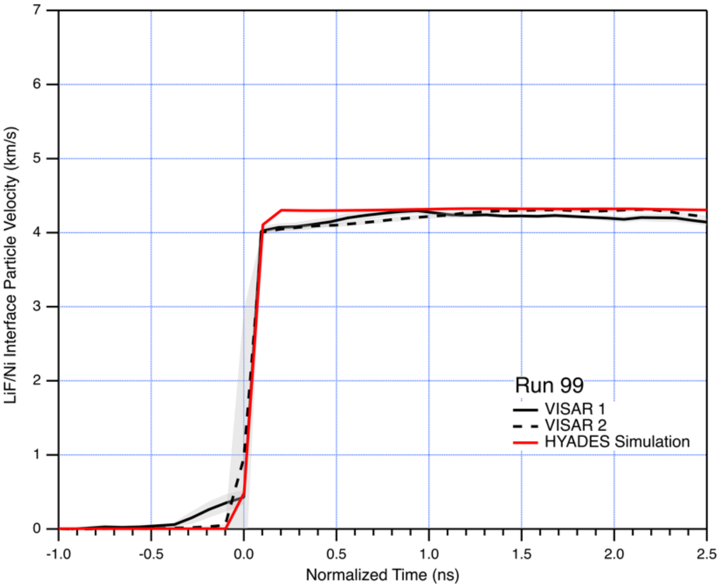

Figure S28. Comparison of experimental VISAR data with calculated particle velocity for the Ni compressed state with a density of 13.44 g/cm^3 (refined from the XRD data). Simulation of particle velocity versus time at the Ni/LiF interface for Run 099 uses the HYADES package. Breakout occurs at the sharp increase in particle velocity, followed by a plateau. Simulations were calculated using equations of state from the SESAME database (83103 for Ni [17], 7271 for LiF, and 7770 for Kapton [20]).

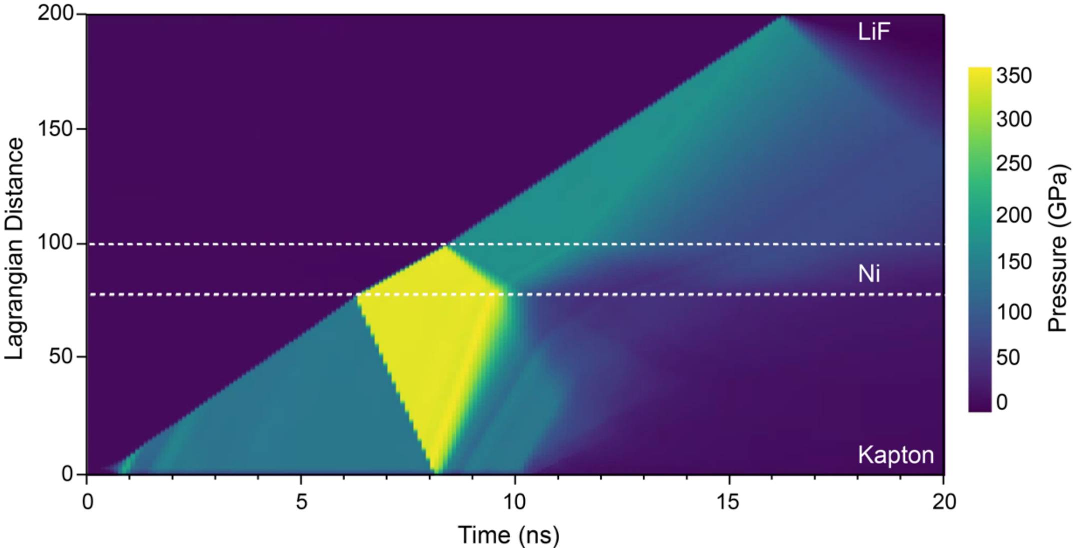

Figure S29. Plot of the 1D hydrocode simulations carried out for Run 160 using the HYADES package. Different layers of the sample are labelled, with dashed white lines denoting the interfaces. The simulations were designed to match the density obtained from the Rietveld refinements of the X-ray diffraction data. Pressures reached in the sample are plotted by color, with the corresponding color bar legend shown on the right. Simulations were calculated using equations of state from the SESAME database (83103 for Ni [17], 7271 for LiF and 7770 for Kapton [20]).

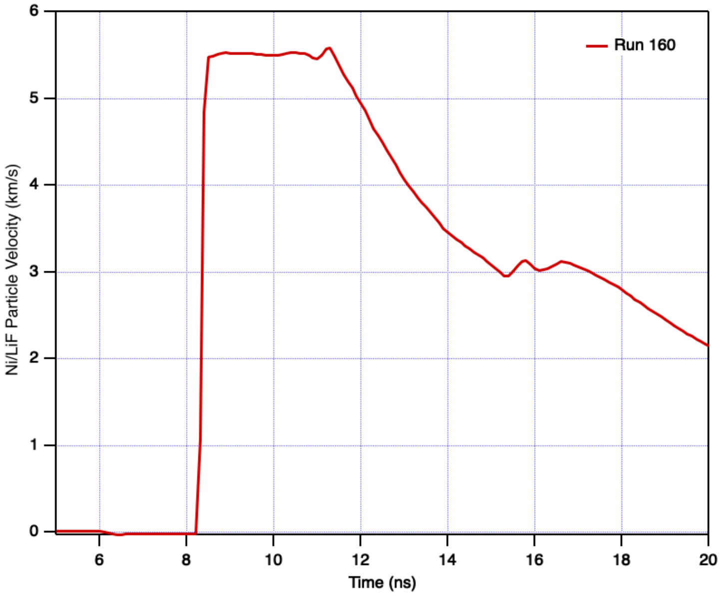

Figure S30. Simulation of particle velocity versus time at the Ni/LiF interface for Run 160 using the HYADES package. Breakout occurs at the sharp increase in particle velocity, followed by a plateau. Simulations were calculated using equations of state from the SESAME database (83103 for Ni [17], 7271 for LiF and 7770 for Kapton [20]).

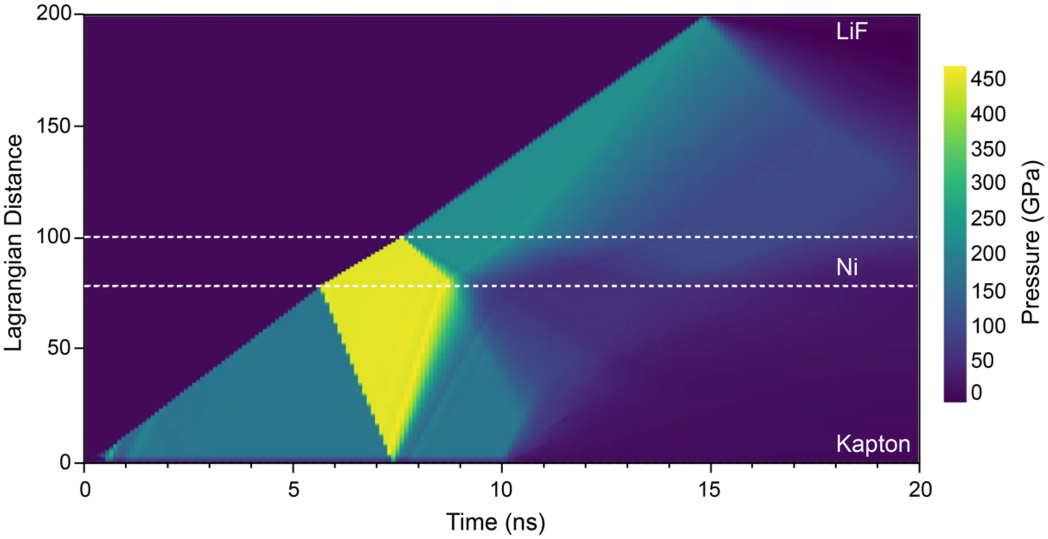

Figure S31. Plot of the 1D hydrocode simulations carried out for Run 151 using the HYADES package. Different layers of the sample are labelled, with dashed white lines denoting the interfaces. The simulations were designed to match the density obtained from the Rietveld refinements of the X-ray diffraction data. Pressures reached in the sample are plotted by color, with the corresponding color bar legend shown on the right. Simulations were calculated using equations of state from the SESAME database (83103 for Ni [17], 7271 for LiF and 7770 for Kapton [20]).

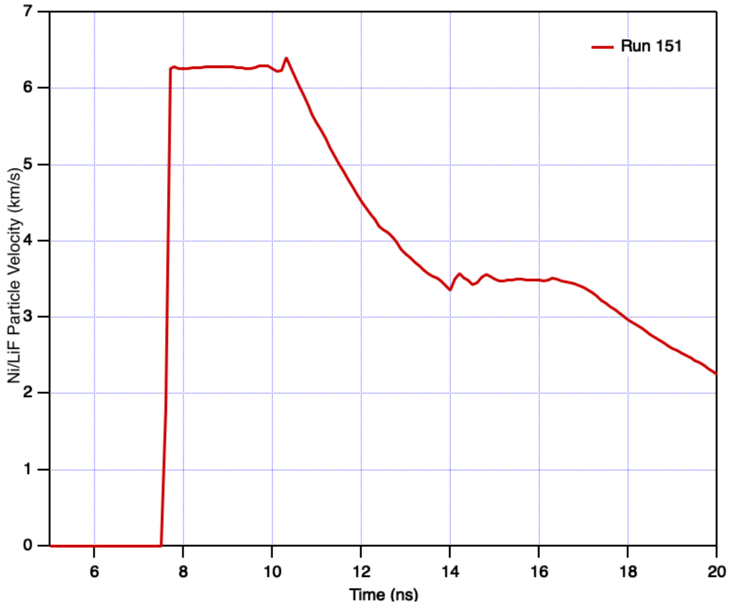

Figure S32. Simulation of particle velocity versus time at the Ni/LiF interface for Run 151 using the HYADES package. Breakout occurs at the sharp increase in particle velocity, followed by a plateau. Simulations were calculated using equations of state from the SESAME database (83103 for Ni [17], 7271 for LiF and 7770 for Kapton [20]).

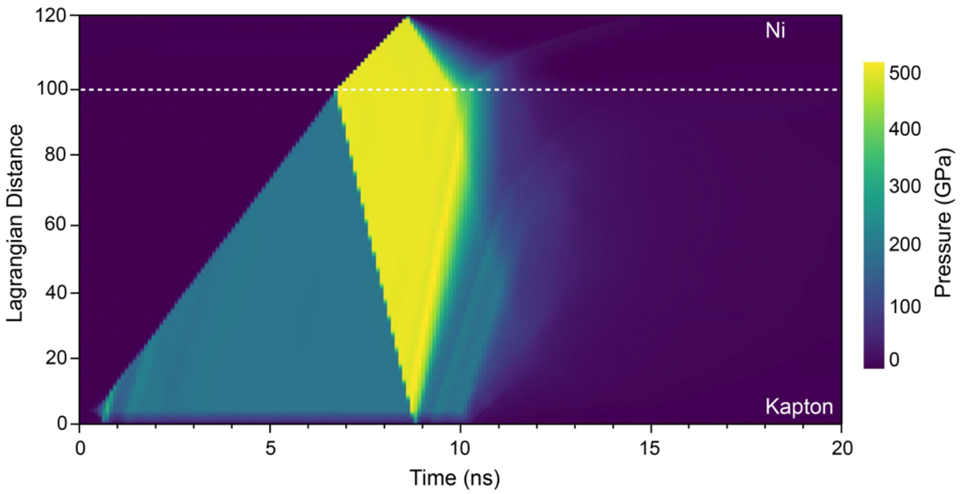

Figure S33. Plot of the 1D hydrocode simulations carried out for Run 420 using the HYADES package. Different layers of the sample are labelled, with dashed white lines denoting the interfaces. The simulations were designed to match the density obtained from the Rietveld refinements of the X-ray diffraction data. Pressures reached in the sample are plotted by color, with the corresponding color bar legend shown on the right. Simulations were calculated using equations of state from the SESAME database (83103 for Ni [17], 7271 for LiF and 7770 for Kapton [20]).

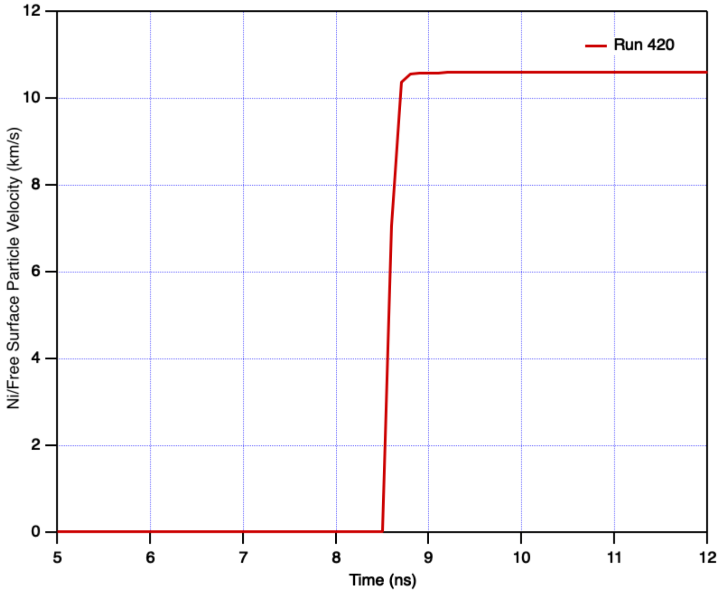

Figure S34. Simulation of particle velocity versus time at the Ni/LiF interface for Run 420 using the HYADES package. Breakout occurs at the sharp increase in particle velocity, followed by a plateau. Simulations were calculated using equations of state from the SESAME database (83103 for Ni [17], 7271 for LiF and 7770 for Kapton [20]).

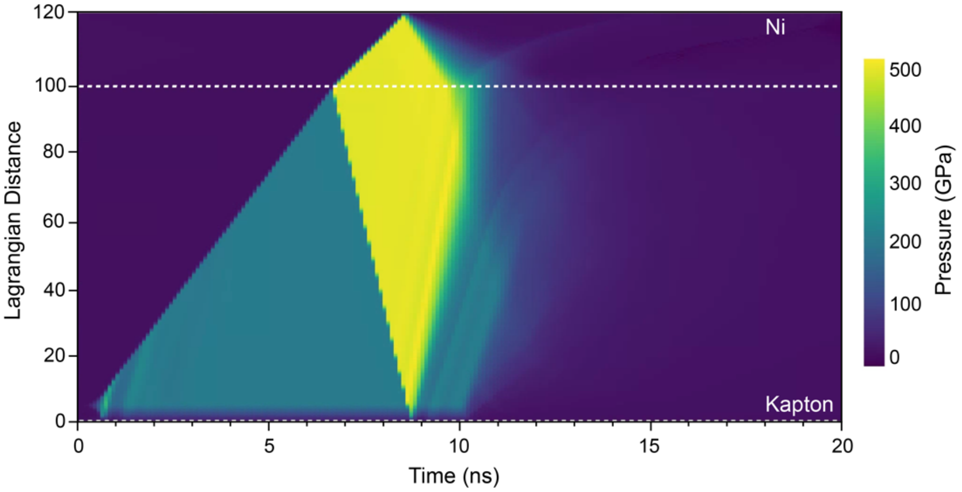

.

Figure S35. Plot of the 1D hydrocode simulations carried out for Run 422 using the HYADES package. Different layers of the sample are labelled, with dashed white lines denoting the interfaces. The simulations were designed to match the density obtained from the Rietveld refinements of the X-ray diffraction data. Pressures reached in the sample are plotted by color, with the corresponding color bar legend shown on the right. Simulations were calculated using equations of state from the SESAME database (83103 for Ni [17], 7271 for LiF and 7770 for Kapton [20]).

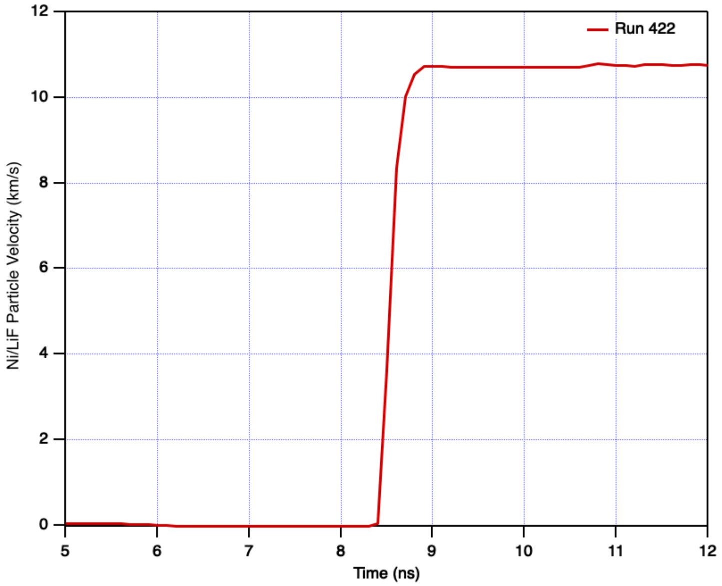

Figure S36. Simulation of particle velocity versus time at the Ni/LiF interface for Run 420 using the HYADES package. Breakout occurs at the sharp increase in particle velocity, followed by a plateau. Simulations were calculated using equations of state from the SESAME database (83103 for Ni [17], 7271 for LiF and 7770 for Kapton [20]).

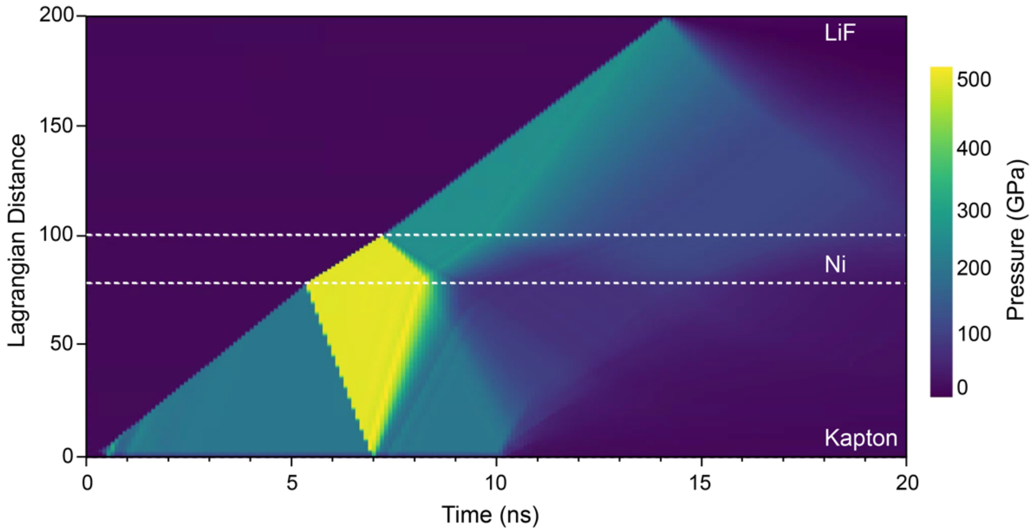

Figure S37. Plot of the 1D hydrocode simulations carried out for Run 149 using the HYADES package. Different layers of the sample are labelled, with dashed white lines denoting the interfaces. The simulation was designed to attain the pressure in the Ni calculated by Equation 3 (506 GPa). Pressures reached in the sample are plotted by color, with the corresponding color bar legend shown on the right. Simulations were calculated using equations of state from the SESAME database (83103 for Ni [17], 7271 for LiF and 7770 for Kapton [20]).

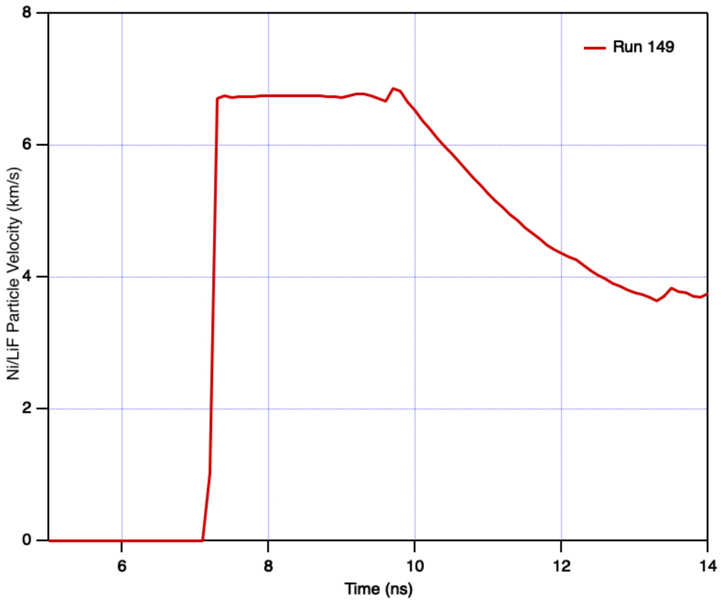

Figure S38. Simulation of particle velocity versus time at the Ni/LiF interface for Run 149 using the HYADES package. Breakout occurs at the sharp increase in particle velocity, followed by a plateau. Simulations were calculated using equations of state from the SESAME database (83103 for Ni [17], 7271 for LiF and 7770 for Kapton [20]).

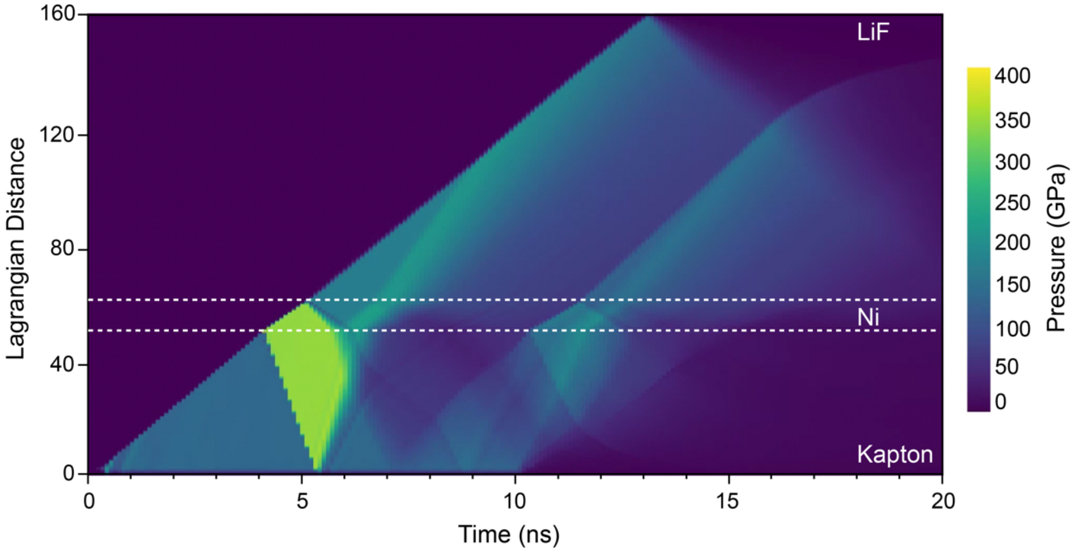

Figure S39. Plot of the 1D hydrocode simulations carried out for Run 493 using the HYADES package. Different layers of the sample are labelled, with dashed white lines denoting the interfaces. The simulations were designed to match the density obtained from the Rietveld refinements of the X-ray diffraction data. Pressures reached in the sample are plotted by color, with the corresponding color bar legend shown on the right. Simulations were calculated using equations of state from the SESAME database (83103 for Ni [17], 7271 for LiF and 7770 for Kapton [20]).

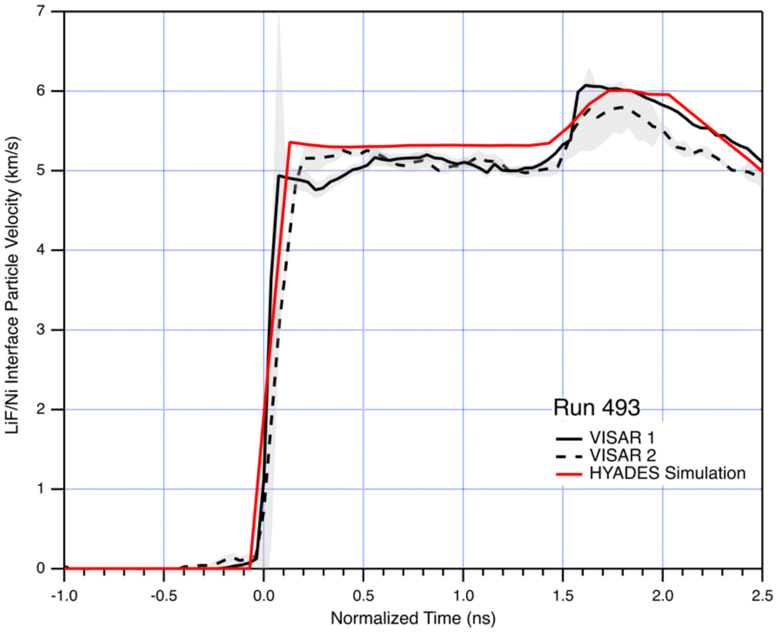

Figure S40. Comparison of experimental VISAR data with calculated particle velocity for the Ni compressed state with a density of 13.97 g/cm^3 (refined from the XRD data). Simulation of particle velocity versus time at the Ni/LiF interface for Run 493 uses the HYADES package. Breakout occurs at the sharp increase in particle velocity, followed by a plateau. Simulations were calculated using equations of state from the SESAME database (83103 for Ni [17], 7271 for LiF and 7770 for Kapton [20]).

References:

[1] P. Lazor, G. Shen, and S. K. Saxena, Phys. Chem. Minerals 20, 86 (1993).

[2] D. Errandonea, B. Schwager, R. Ditz, C. Gessmann, R. Boehler, and M. Ross, Phys Rev B Condens Matter Mater Phys **63**, (2001).

[3] G. I. Kerley, Equations of State for Be, Ni, W, and Au, Report No. SAND-2003-3784, Tech. Rep. (Sandia National Laboratories, 2003).

[4] S. Japel, B. Schwager, R. Boehler, and M. Ross, Phys Rev Lett **95**, (2005).

[5] L. Koči, E. M. Bringa, D. S. Ivanov, J. Hawreliak, J. McNaney, A. Higginbotham, L. V. Zhigilei, A. B. Belonoshko, B. A. Remington, and R. Ahuja, Phys Rev B Condens Matter Mater Phys **74**, (2006).

[6] M. Ross, R. Boehler, and D. Errandonea, Phys Rev B Condens Matter Mater Phys **76**, (2007).

[7] D. Errandonea, Phys Rev B Condens Matter Mater Phys **87**, (2013).

[8] M. Pozzo and D. Alfè, Phys Rev B Condens Matter Mater Phys **88**, (2013).

[9] O. T. Lord, I. G. Wood, D. P. Dobson, L. Vočadlo, W. Wang, A. R. Thomson, E. T. H. Wann, G. Morard, M. Mezouar, and M. J. Walter, Earth Planet Sci Lett **408**, 226 (2015).

[10] H. K. Hieu, J Appl Phys **116**, (2014).

[11] W. J. Zhang, Z. L. Liu, and Y. F. Peng, Physica B Condens Matter **449**, 144 (2014).

[12] D. V. Minakov and P. R. Levashov, Phys Rev B Condens Matter Mater Phys **92**, (2015).

[13] Q. L. Cao, P. P. Wang, D. H. Huang, J. S. Yang, M. J. Wan, and F. H. Wang, Chinese Physics Letters **32**, (2015).

[14] S. Boccato, R. Torchio, I. Kantor, G. Morard, S. Anzellini, R. Giampaoli, R. Briggs, A. Smareglia, T. Irifune, and S. Pascarelli, J Geophys Res Solid Earth **122**, 9921 (2017).

[15] N. Quang Hoc, T. Dinh Cuong, B. Duc Tinh, and L. Hong Viet, Modern Physics Letters B **33**, (2019).

[16] D. K. Belashchenko, High Temperature **58**, 64 (2020).

[17] T. Sjostrom, Sesame Equation of State for Nickel, Report No. LA-UR-22-21603, Tech. Rep., (Los Alamos National Laboratory, 2022).

[18] C. J. Prisbrey, P. Soderlind, and C. J. Wu, A New Multiphase Equation of State Table for Ni, Report No. LLNL-PROC-856971, Tech. Rep., (Lawrence Livermore National Laboratory, 2023).

[19] N. A. Smirnov, J Appl Phys **134**, (2023).

[20] S. P. Lyon and J. D. Johnson, “Sesame: The Los Alamos National Laboratory Equation of State Database,” Report No. LA-UR-92-3407, Tech. Rep. (Los Alamos National Laboratory, 1992).

[21] J. M. Walsh, M. H. Rice, R. G. Mcqueen, and F. L. Yarger, Physical Review **108**, 195 (1957).

[22] R. G. McQueen and S. P. Marsh, J Appl Phys **31**, 1253 (1960).

[23] S. B. Kormer, A. I. Funtikov, V. D. Urlin, and A. N. Kolesnikova, DYNAMIC COMPRESSION OF POROUS METALS AND THE EQUATION OF STATE WITH VARIABLE SPECIFIC HEAT AT HIGH TEMPERATURES, 1962.

[24] L. V Al’tshuler, A. A. Bakanova, and R. F. Trunin, Shock Adiabats and Zero Isotherms of Seven Metals at High Pressures, 1962.

[25] W. M. Isbell, F. H. Shipman, and A. H. Jones, Hugoniot Equation of State for Eleven Materials to Five Megabars, 1968.

[26] S. P. Marsh, LASL Shock Hugoniot Data, (University of California Press, Berkeley, CA, 1980).

[27] L. V. Al’tshuler, A. A. Bakanova, I. P. Dudoladov, E. A. Dynin, R. F. Trunin, and B. S. Chekin, Journal of Applied Mechanics and Technical Physics **22**, 145 (1981).

[28] R. F. Trunin, G. V Sirnakov, Y. N. Sutulov, A. B. Medvedev, B. D. Rogozkin, and Y. E. Fedorov, Compressibility of Porous Metals in Shock Waves, 1989.

[29] T. B. van Driel, S. Nelson, R. Armenta, G. Blaj, S. Boo, S. Boutet, D. Doering, A. Dragone, P. Hart, G. Haller, C. Kenney, M. Kwaitowski, L. Manger, M. McKelvey, K. Nakahara, M. Oriunno, T. Sato, and M. Weaver, J Synchrotron Radiat **27**, 608 (2020).

[30] J. Kieffer and J. P. Wright, Powder Diffr **28**, S339 (2013).

[31] G. Ashiotis, A. Deschildre, Z. Nawaz, J. P. Wright, D. Karkoulis, F. E. Picca, and J. Kieffer, J Appl Crystallogr **48**, 510 (2015).

[32] J. Wang, F. Coppari, R. F. Smith, J. H. Eggert, A. E. Lazicki, D. E. Fratanduono, J. R. Rygg, T. R. Boehly, G. W. Collins, and T. S. Duffy, Phys Rev B Condens Matter Mater Phys **92**, (2015).

[33] P. Renganathan, S. J. Turneaure, S. M. Sharma, and Y. M. Gupta, Phys Rev B **99**, (2019).

[34] S. Singh, R. Briggs, M. G. Gorman, L. X. Benedict, C. J. Wu, S. Hamel, A. L. Coleman, F. Coppari, A. Fernandez-Pañella, C. McGuire, M. Sims, J. K. Wicks, J. H. Eggert, D. E. Fratanduono, and R. F. Smith, Phys Rev B **108**, (2023).
[35] R. P. Drake, *High-Energy-Density Physics* (Springer Berlin Heidelberg, 2006).
[36] J. Lindl, Phys Plasmas **2**, 3933 (1995).
[37] S. B. Brown, A. Hashim, A. Gleason, E. Galtier, I. Nam, Z. Xing, A. Fry, A. Mackinnon, B. Nagler, E. Granados, and H. J. Lee, Review of Scientific Instruments **88**, (2017).
[38] J. T. Larsen and S. M. Lane, J Quant Spectrosc Radiat Transf **51**, 179 (1994).